

New Bayesian algorithm for sea ice detection with QuikSCAT

Maria Belmonte Rivas, Ad Stoffelen

Abstract—The authors propose a new sea ice detection method for a rotating Ku-band scatterometer with dual polarization capability, such as Seawinds on QuikSCAT, based on probabilistic distances to ocean wind and sea ice Geophysical Model Functions (GMFs) and evaluate its performance against other active and passive microwave algorithms. All the methods yield similar results during the sea ice growth season, but show substantial differences during the spring and summer months. A detailed comparison based on high resolution SAR and optical imagery shows that major discrepancies relate to newly formed, low concentration and water saturated sea ice species. The new GMF-based algorithm for sea ice detection with QuikSCAT improves on the misclassification scores that affect other algorithms and provides daily sea ice masks at 25 km resolution for use in ground processors that require the effective removal of sea ice contaminated pixels all year round.

Index Terms— Sea ice, spaceborne radar, Bayesian methods, radar scattering, microwave radiometry.

I. INTRODUCTION

IN 2007, the summer extent of Arctic sea ice observed by satellite sensors reached its lowest value on record since 1979 [1]. Satellite platforms provide a convenient way to monitor the vast expanses of sea ice in the Polar Regions, mainly thanks to microwave sensors which, contrary to optical techniques, can operate at night and in all-weather conditions. The determination of sea ice extents from satellite platforms is exploited as a marker for climate change, a navigation aid and a validation tool in cryospheric modelling studies. Sea ice detection is routinely performed by two types of sensors: passive microwave radiometers, which observe the natural emissions from the Earth's surface [2], and active microwave scatterometers, which collect the energy reflected from an initially transmitted pulse [3]–[5]. Earlier studies have shown a reasonable agreement between scatterometer and radiometer sea ice extents [6] with remarkable seasonal discrepancies roughly characterized by defective scatterometer extents during the sea ice growth season [7] and defective radiometer extents during the summer months [8]. In this paper, we revisit the determination of sea ice extents using satellite

microwave sensors, propose an improved method for sea ice detection using the Seawinds scatterometer on QuikSCAT and evaluate its performance against other active and passive microwave records across the sea ice growth and melt cycles.

Section II details the construction and underlying principles of the Geophysical Model Function (GMF) based sea ice detection method for QuikSCAT. In Section III, we cross-examine the location of the resulting ice edge against the sea ice concentration from the AMSR-E (Advanced Microwave Scanning Radiometer) Enhanced NASA Team (NT2) algorithm and the QuikSCAT Scatterometer Climate Record (SCP). The extent and nature of the discrepancies observed are analyzed using higher resolution optical and synthetic aperture radar (SAR) data. Section IV summarizes our results and concludes with notes on future work.

II. ALGORITHM DESCRIPTION

Scatterometers are active microwave sensors whose primary mission consists in the determination of surface winds over the oceans. The QuikSCAT scatterometer radiates microwave pulses at a frequency of 13.4 GHz and employs a rotating dish antenna for the reception of horizontally and vertically polarized returns from two incidence and four azimuth angles, providing a diversity of views that allows for the detection of the wind vector signature over open water (Fig.1).

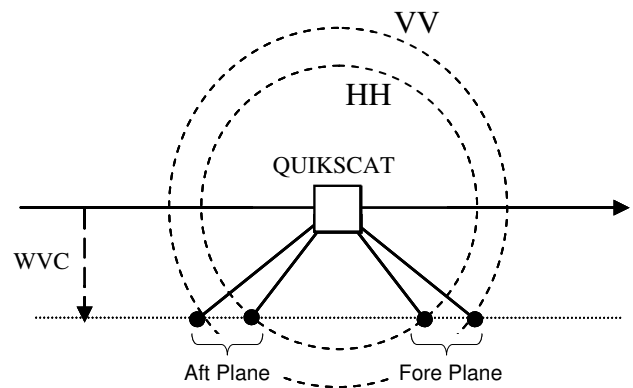
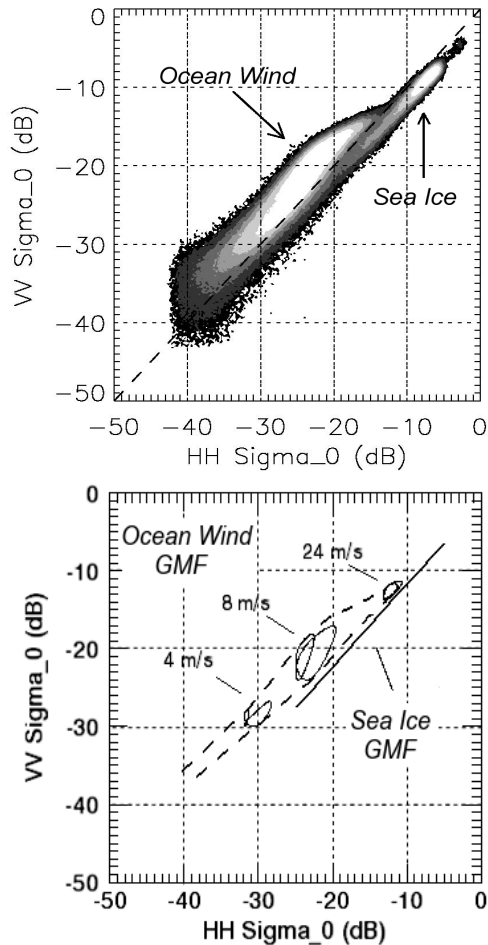


Fig. 1. Top view of QuikSCAT observation geometry. The sensor provides a sequence of $N = 4$ backscatter views per Wind Vector Cell (WVC), or $\{\sigma^0\} = [\sigma_{VV\text{-fore}}^0, \sigma_{HH\text{-fore}}^0, \sigma_{HH\text{-aft}}^0, \sigma_{VV\text{-aft}}^0]$. The incidence angles for the inner HH and outer VV polarized beams are 46° and 54° respectively. The angle between the fore and aft planes depends on WVC location.

An inspection of the distribution of backscatter points from open water and sea ice surfaces in the QuikSCAT backscatter space reveals that they occupy largely distinct sectors (see 2D histogram on top panel in Fig.2). While surface scattering from a wind roughened patch of open water is characterized by marked polarization ($\sigma_{VV} > \sigma_{HH}$) and azimuthal anisotropy ($\sigma_{VV,fore} \neq \sigma_{VV,aft}$), volume scattering from a sea ice slab results in depolarized, azimuth invariant and usually stronger returns.



$$\begin{aligned} \{\sigma_{wind}^0\} &= \mathbf{GMF}_{wind}(\text{wind speed, wind direction, WVC}) \\ \{\sigma_{ice}^0\} &= \mathbf{GMF}_{ice}(\text{ice brightness}) \end{aligned}$$

Fig. 2. Observed distribution of backscatter (TOP) and empirical ocean wind and sea ice model functions (BOTTOM) in the space of QuikSCAT measurements (projection on the for/aft planes).

The first sea ice detection algorithms with scatterometer data relied on hard-threshold tests that capitalized on these properties. They evolved in time into maximum likelihood (Bayesian) methods with separate class cluster centroids for mean backscatter $\langle \sigma_{HH} \rangle$, polarization ratio $\sigma_{VV,fore} / \sigma_{HH,fore}$ and azimuthal anisotropy $\Delta \sigma_{HH} = \sqrt{[\sigma_{HH,fore}^2 - \sigma_{HH,aft}^2]}$ (or $\Delta \sigma_{VV}$) acting as discriminant parameters, and jointly Gaussian [3] or empirically adjusted [4] covariances characterizing the dispersion of these aggregates about their class centroids. The new GMF-based approach reverts the Bayesian classification back to the measurement space by replacing the former class

centroids for mean backscatter, polarization and anisotropy by extended Geophysical Model Functions (GMFs) for ocean wind and sea ice backscatter at Ku-band [9].

A. Geophysical Model Functions (GMFs)

The GMFs are empirically derived functions that relate backscatter measurements to surface conditions observed from a variety of incidence and azimuth angles. For a given observation geometry, the backscatter from the ocean surface is determined by wind speed and direction, tightly conforming to a two-dimensional manifold in the multi-dimensional space of backscatter views collected per Wind Vector Cell (WVC). The bottom panel on Fig.2 shows the projection of the tube-shaped ocean wind manifold on the fore/aft backscatter planes of QuikSCAT (σ_{HH} vs. σ_{VV} , see in Fig.1). The variability of ocean backscatter with wind direction is outlined in Fig.2 by slices across the ocean wind manifold for a limited set of windspeeds (4, 8 and 24 m/s) for an outer swath WVC. Changes in wind direction will make ocean backscatter fan out along these curves, adding to the observed spread in ocean polarization ratio. Observe that the relative azimuth angle between the scatterometer beams varies with WVC location (see Fig.1), slightly altering the shape of the ocean wind manifold and the subsequent spread in ocean polarization over the QuikSCAT swath. The backscatter from a sea ice surface, on the other hand, is azimuth (and WVC) invariant, tightly conforming to a one-dimensional straight line model that features sea ice brightness (or proxy sea ice age) as its only independent variable, also shown in Fig. 2.

The empirical GMF for ocean wind σ_{wind}^0 was developed and is applied operationally to retrieve wind vectors over open water surfaces, generally fitting observations to within instrumental noise levels. It was determined after a statistical comparison between ADEOS NSCAT 14 GHz dual-polarized backscatter measurements and collocated ECMWF NWP winds [10], and is currently available in tabulated form at www.knmi.nl/scatterometer. The empirical GMF for sea ice σ_{ice}^0 has been drawn from the observed distribution of winter 100% concentration sea ice backscatter [11], which clusters along a straight line in the four-dimensional QuikSCAT dB-space. The brightness of sea ice backscatter may vary substantially across the seasons, but its HH and VV polarized components maintain a fixed proportion ($\sigma_{VV,dB} = 1.06 \cdot \sigma_{HH,dB} - 1.0$) regardless of azimuth angle ($\sigma_{VV,fore} = \sigma_{VV,aft}$ and $\sigma_{HH,fore} = \sigma_{HH,aft}$). These facts can be verified statistically down to instrumental noise levels (~ 0.5 dB one-sigma for QuikSCAT, including thermal and speckle noise contributions) indicating that the variance of pure sea ice backscatter about (read *away from*) the linear sea ice model is commensurate with instrumental noise (see Fig.3A [11]). The advantage of the GMF-based approach relative to the former cluster methods is that the dispersion of measurements about extended model functions is smaller than that about class cluster centroids, actually approaching the limits imposed by the scatterometer noise levels and allowing the Bayesian methodology to reach its full discrimination power.

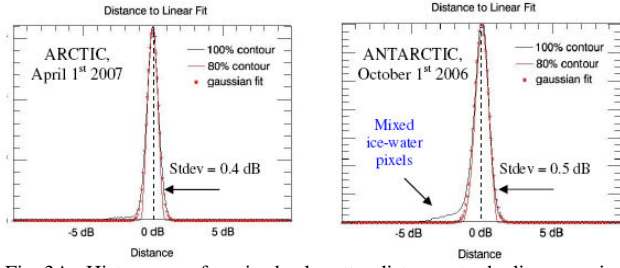


Fig. 3A. Histograms of sea ice backscatter distances to the linear sea ice GMF on the QuikSCAT fore/aft backscatter planes. Lines are drawn for 100% and 80% histogram contours, with a best fit Gaussian curve superimposed.

B. Maximum Likelihood Estimators (MLEs)

The GMF-based algorithm computes the minimum squared distances (or MLE, from maximum likelihood estimators) to the ocean wind σ^0_{wind} and sea ice σ^0_{ice} model functions as:

$$MLE_{wind} = \sum_{i=1, \dots, N} (\sigma_i^0 - \sigma_{wind,i}^0)^2 / \text{var}[\sigma_{wind,i}^0] \quad (1)$$

$$MLE_{ice} = \sum_{i=1, \dots, N} (\sigma_i^0 - \sigma_{ice,i}^0)^2 / \text{var}[\sigma_{ice,i}^0] \quad (2)$$

where i is an index to the components of the backscatter vector and N is its dimension (or number of views per cell, $N = 4$ for QuikSCAT) and the normalizing factors $\text{var}[\sigma_{class,i}^0]$ guarantee that the variance of backscatter components about the corresponding model function is unity. The variance of measurements about the ocean wind GMF is a well known parameter and expressed as the sum of instrumental K_p and geophysical K_{geo} random Gaussian components as:

$$\text{var}[\sigma_{wind}^0] = (K_p^2 + K_{geo}^2) \sigma_{wind}^0{}^2 \quad (3)$$

The instrumental K_p noise refers to radiometric uncertainty in the Seawinds receiver chain [12] with a best case value of 10% at high winds, as reported in the QuikSCAT products. The geophysical K_{geo} noise is a lumped concept that accounts for perturbations in ocean wind backscatter due to non-instrumental causes such as wind variability, atmospheric instability or undetected rain [13] with a best case value of 5% at high winds, as estimated in [14]. The parameters K_p and K_{geo} are currently tabulated as a function of backscatter strength and available at www.knmi.nl/scatterometer. The variance of pure (100% concentration) sea ice backscatter about the sea ice GMF is commensurate with the instrumental noise K_p , but the increased variance of backscatter from lower sea ice fractions may require the use of a tolerance factor C_{mix} :

$$\text{var}[\sigma_{ice}^0] = (C_{mix} K_p \sigma_{ice}^0)^2 \quad (4)$$

This tolerance factor C_{mix} deals with excursions away from the sea ice model that go beyond instrumental noise expectations. These excursions are typically observed when both sea ice and open water signatures are present in a resolution cell. Increasing C_{mix} should widen the tolerance to excursions from the sea ice model and lead to a better capture of mixed surface conditions, which are pervasive during the summer months and along the Antarctic sea ice margin all year round. The tolerance factor is to be adjusted empirically against a valid reference in the next section.

Under a Gaussian noise assumption, the minimum squared distance MLE defined in (1) and (2) becomes the sum of N squared standard Gaussian variables. The sum is equivalent to a chi-square random variable with $N-Q$ degrees of freedom, where Q is the number of linear constraints imposed on the sum by the GMF fitting process: note that the distance minimization absorbs one degree of statistical freedom per model dimension. The Gaussian noise components absorbed by (i.e. parallel to) the GMF become errors in the retrieved model parameters (wind vector or sea ice brightness), leaving those components orthogonal to the GMF as sole contributors to the minimum squared distance. The expected distributions of minimum squared distances to the 2D ocean wind GMF ($Q = 2$) and 1D sea ice GMF ($Q = 1$) can be therefore modeled as chi-square functions with $N-2$ and $N-1$ degrees of freedom:

$$p(MLE_{ice}) = \sqrt{\frac{MLE_{ice}}{2\pi}} \exp(-MLE_{ice}/2) \quad (5)$$

$$p(MLE_{wind}) = \frac{1}{2} \exp(-MLE_{wind}/2) \quad (6)$$

The expected distributions of minimum square distances MLE to the QuikSCAT ocean wind and sea ice GMFs are verified against actual measurement distributions in Fig. 3B. Note that the observed MLE distributions follow the expected chi-square functions closely.

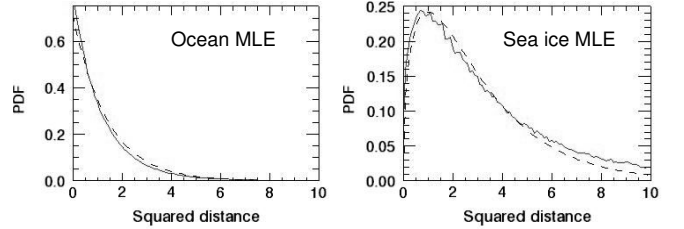


Fig. 3B. Observed (continuous) and expected (dashed) MLE distributions to the ocean wind (LEFT) and sea ice (RIGHT) GMFs. For reference, instrumental noise is $K_p \sim 10\%$ or about 0.5 dB (1σ) over most of the QuikSCAT dynamic range and $C_{mix}=1$.

C. Bayesian prior and posterior probabilities

Once we know the expected location and dispersion of the sea ice and open water backscatter populations in the QuikSCAT measurement space, we can proceed to establish a Bayesian decision rule. The Bayesian posterior sea ice probability is formulated as:

$$p(ice | \sigma^0) = \frac{p(\sigma^0 | ice) p_0(ice)}{p(\sigma^0 | ice) p_0(ice) + p(\sigma^0 | wind) p_0(wind)} \quad (7)$$

in terms of prior historic information $p_0(ice)$ and $p_0(wind)$, and the conditional probability distributions of minimum squared distances $p(\sigma^0 | wind)$ and $p(\sigma^0 | ice)$ to the sea ice and ocean wind model functions, defined as:

$$\begin{aligned} p(\sigma^0 | ice) &= p(MLE_{ice}) \\ p(\sigma^0 | wind) &= p(MLE_{wind}) \end{aligned} \quad (8)$$

An important weakness in this formulation is the loss of discrimination power at locations where class GMFs intersect one another. In our case, the bright tail of the sea ice model approaches the high wind portion of the ocean wind model

(see Fig. 2). As a consequence, bright multiyear ice is likely to be interpreted as a strong ocean wind, and vice versa. To relieve this problem, we introduce a prior constraint based on Numerical Weather Prediction (NWP) forecasts of the surface wind v_{NWP} . This constraint assigns low prior probabilities to apparent GMF ocean winds v that deviate largely from the NWP forecast v_{NWP} following:

$$p(\sigma^0 | wind) = p(MLE_{wind}) \cdot \exp(-|\bar{v} - \bar{v}_{NWP}|^2 / 2\Delta v^2) \quad (8a)$$

where $\Delta v = 5$ m/s using ECMWF short-range wind forecasts. This addition prevents bright ice from being interpreted as a strong wind, while it does generally not introduce false sea ice artifacts in other regions.

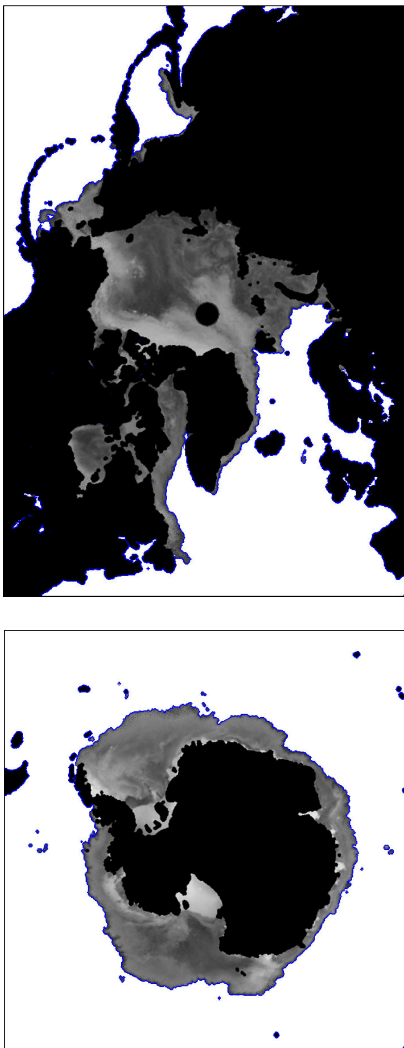


Fig. 4. Sample Arctic and Antarctic sea ice extents for March 21st 2007 from the QSCAT-KNMI algorithm using a sea ice GMF $\text{std}[\sigma_{ice}^0] = 1.5$ dB. Background grey scale represents sea ice brightness or proxy sea ice age.

The prior sea ice and ocean wind probabilities are set initially to $p_0(ice) = 0.50 = 1 - p_0(wind)$, updated every orbit using the previous pass posteriors as $p_0(ice) = p(ice | \sigma^0) = 1 - p_0(wind)$, and relaxed daily towards uncertainty following:

$$p_0(ice) = \begin{cases} 0.50 & \text{if } p(ice | \sigma^0) > 0.30 \\ 0.15 & \text{if } p(ice | \sigma^0) < 0.30 \end{cases} \quad (9)$$

These settings are found to maximize the quality of the prior information used for sea ice detection, and efficient at inhibiting rain contamination effects. The Bayesian algorithm implemented at KNMI generates near-real time daily sea ice masks with NRT QuikSCAT L2B BUFR data [15] using a 55% threshold to posterior sea ice probabilities in (7). The sea ice masks are filled with backscatter strength values indicative of ice age/thickness (Fig. 4) and finally archived.

III. ALGORITHM VALIDATION

Our validation work begins with the collection of a continuous series of sea ice extents as recorded by the passive microwave AMSR-E sensor during the period from September 2006 to September 2007. The passive microwave sea ice extents are defined by the 15% isoline on daily sea ice concentrations generated by the NT2 algorithm (AE SI12 V1, [16], [17], [18]). The location of the passive microwave 15% isoline has been carefully validated against MODIS and RADARSAT imagery [21] and widely used as a reference sea ice edge by many other authors. The AMSR-NT2 15% isoline currently provides the best available representation of sea ice edge in the wintertime, although it is known to be less reliable during the spring and summer months due to weather effects, unresolved ice types and surface melt conditions [16].

As a preliminary step, we adjust the tolerance factor C_{mix} of the GMF-based sea ice detection algorithm (QSCAT-KNMI) using the wintertime AMSR-NT2 sea ice extents as reference. This exercise also illustrates the sensitivity of the new method to the expected dispersion of backscatter about the sea ice model. The GMF-based algorithm is run using different tolerance factors ($C_{mix} = 1, 2$ and 3) and the results shown in Fig. 6. The comparison is performed on a 12.5 km polar stereographic grid with a common landmask and a 25 km coastal buffer. As expected, the total extent of sea ice detected by QuikSCAT increases with the tolerance factor, showing a larger sensitivity at definite geographical locations (like the Antarctic sea ice margin) and certain times of the year (like the Arctic spring and summer months). This sensitivity is naturally confined to areas where mixed sea ice and open water conditions are frequent, and mainly include i) low concentration sea ice in marginal ice zones, ii) water saturated sea ice in the melt season, and iii) partly translucent thin ice rapidly formed in the fall months.

The mixed surface/volume scattering signature induced by rain cannot be well separated from that of thin or low concentration sea ice in terms of Seawinds backscatter alone, and constitutes a serious source of misclassification noise at Ku-band. Fig. 5 illustrates the evolution of rain polluted ocean backscatter on the fore/aft backscatter planes of QuikSCAT as the precipitation rate increases (c.f. Fig. 2) [19]. The rain signature appears to dominate the ocean backscatter signature gradually, particularly at low winds, and more effectively so as the precipitation rate increases, drawing measurements

towards the region occupied by the sea ice GMF, that is the region occupied by depolarized and azimuthally invariant backscatter.

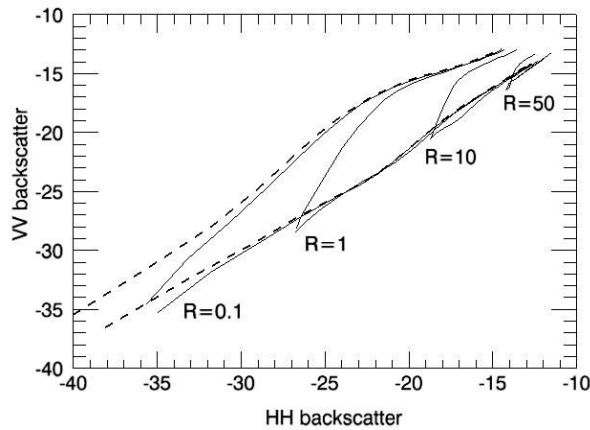


Fig. 5 Evolution of rain polluted ocean backscatter on the fore/aft backscatter planes of QuikSCAT (the dashed line shows the projection of the uncontaminated ocean wind GMF). R is columnar rain rate in km-mm/hr, as taken from [19].

To increase the inclusiveness of the GMF-based QuikSCAT algorithm to thin and low concentration sea ice species, the tolerance to mixed ice/water conditions should be increased up to the point where misclassification noise due to rain starts to be noticed. The utilization of a lower tolerance factor would improve the rain rejection properties of the algorithm, but would also give way to defective scatterometer extents during the sea ice growth season, when partly translucent thin ice is most prevalent (see the upward branches in Fig 6). The comparison against the reference AMSR-NT2 15% sea ice concentration during the fall and winter months leads to an optimal $C_{mix} = 3$ with $\text{std}[\sigma_{ice}^0] = 1.5$ dB. The optimal configuration run of the GMF-based algorithm also indicates that passive microwave extents are biased low relative to QuikSCAT in the spring and summer months (see the downward branches in Fig. 6).

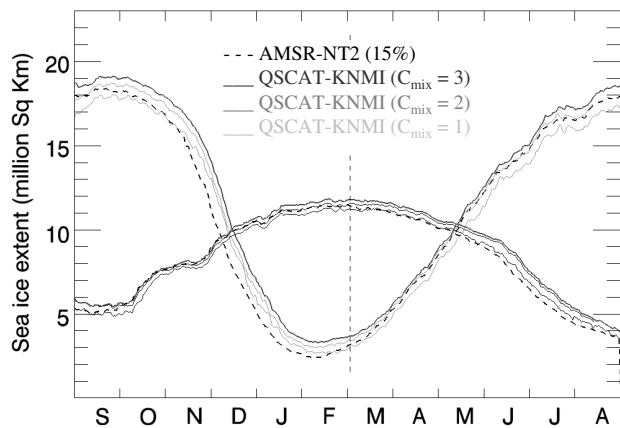


Fig. 6 Daily Arctic and Antarctic sea ice extents for Sep'06 to Sep'07 from radiometer (AMSR-NT2, dashed line) and scatterometer (QSCAT-KNMI, shaded lines) using different sea ice model variances ($\text{std}[\sigma_{ice}^0] = 0.5, 1.0$ and 1.5 dB)

Another validation source is provided by the QuikSCAT cluster centroid method, denoted QSCAT-SCP (Scatterometer Climate Pathfinder record, V2) [3]. The QSCAT-SCP method is compared against the AMSR-NT2 and the optimal GMF-based QSCAT-KNMI algorithms from September 2006 to September 2007 in Fig. 7, to show good agreement during fall and winter in both hemispheres, but large discrepancies as the spring melt sets in. Some quantitative details of this comparison are given in Table 1, including a formal estimation of the algorithm variance about the three-algorithm ensemble. Two important points to note: a) the biases in total sea ice extent between algorithms are larger in spring and summer, up to 20% between active and passive microwave methods, pointing at their differing ability to detect sea ice in the difficult spring melt conditions, and b) the formal dispersion about the algorithm ensemble, which provides an indication of the random day-to-day variability due to misclassification noise, is largest in spring and summer, and largest for the QSCAT-SCP method during the stormy Arctic fall and winter months (see square box in Fig. 7).

TABLE I
MEAN SEASONAL ARCTIC/ANTARCTIC SEA ICE EXTENTS

Arctic ($\times 10^6$ km 2)	QSCAT-KNMI	QSCAT-SCP	AMSR-NT2
Fall/OND	7.79 ± 0.09	7.84 ± 0.15	7.72 ± 0.07
Winter/JFM	9.91 ± 0.05	9.90 ± 0.09	9.74 ± 0.05
Spring/AMJ	9.75 ± 0.09	9.55 ± 0.06	9.39 ± 0.06
Summer/JAS	6.24 ± 0.13	5.91 ± 0.12	5.40 ± 0.09

Antarctic ($\times 10^6$ km 2)	QSCAT-KNMI	QSCAT-SCP	AMSR-NT2
Spring/OND	15.85 ± 0.34	14.89 ± 0.18	14.19 ± 0.41
Summer/JFM	4.50 ± 0.29	3.84 ± 0.21	3.40 ± 0.25
Fall/AMJ	8.51 ± 0.06	8.40 ± 0.07	8.20 ± 0.04
Winter/JAS	16.49 ± 0.11	16.15 ± 0.11	15.97 ± 0.07

The formal dispersion (1σ) is calculated about the three-algorithm ensemble, after removal of a smooth cubic polynomial bias.

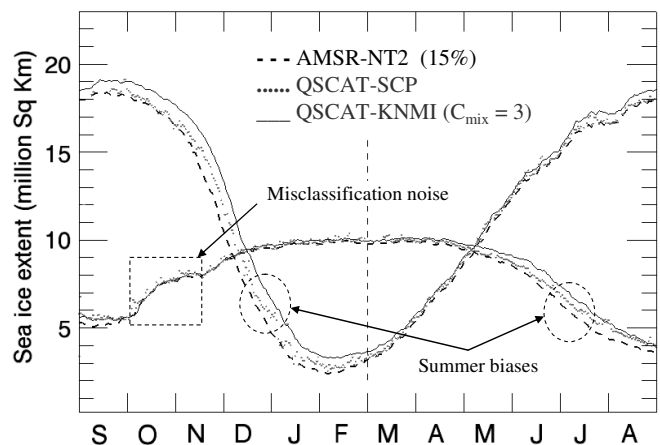


Fig. 7. Daily Arctic and Antarctic sea ice extents for Sep'06 to Sep'07 from radiometer (AMSR-NT2, dashed line) and scatterometer (QSCAT-KNMI 1.5 dB, continuous line and QSCAT-SCP, dotted line)

Day-to-day dispersion due to misclassification noise may not be as problematic as the total sea ice extent biases observed in the summer, but remains an important quality indicator. Misclassification noise in the QSCAT-KNMI algorithm is mainly caused by rain contaminated pixels, and it is largely suppressed by the Bayesian combination of measurements and a priori information, whereas the QSCAT-SCP algorithm is affected over more extended areas that include both rain contaminated and wind roughened ocean surfaces. Misclassification noise in AMSR-NT2 relates to uncorrected atmospheric cloud liquid and water vapor effects and is very low.

A comparison of the average passive microwave sea ice concentration evaluated at the QSCAT-SCP and QSCAT-KNMI ice edges provides further evidence of their relative performance. The mean sea ice concentration at the QSCAT-SCP winter edge is about 25-30%, while the QSCAT-KNMI method stretches out to the 10-15% concentration levels at the winter edge, falling slightly behind the AMSR-NT2 reference during the dynamic Arctic growth season (see Fig. 8). In the light of this comparison, we conclude that the QSCAT-KNMI algorithm performs better than the QSCAT-SCP method in the detection of newly formed thin ice during the winter months.

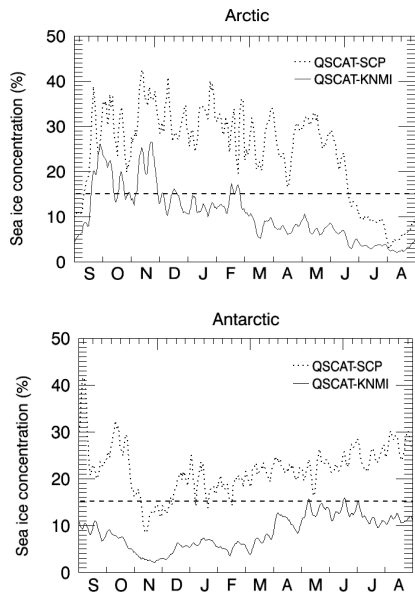


Fig. 8. Daily average AMSR-NT2 sea ice concentration along the QSCAT-SCP and QSCAT-KNMI ice/ocean boundaries over the Arctic (TOP) and Antarctic (BOTTOM) regions from Sep'06 to Sep'07.

The reference wintertime AMSR-NT2 15% isoline is highlighted.

Another issue with the QSCAT-SCP method is that it does not attempt to detect water openings in the ice pack (a.k.a. polynyas). This problem has been addressed in later and improved versions of the cluster centroid method (see e.g. [4] or [20] with enhanced-resolution QuikSCAT data), but the average sea ice concentration at the ice edge remains similar to what is reported here for QSCAT-SCP. The very low equivalent passive microwave sea ice concentration observed at the scatterometer edge in the spring and summer months in Fig. 8 is indicative of defective radiometer estimates, a point that is addressed next.

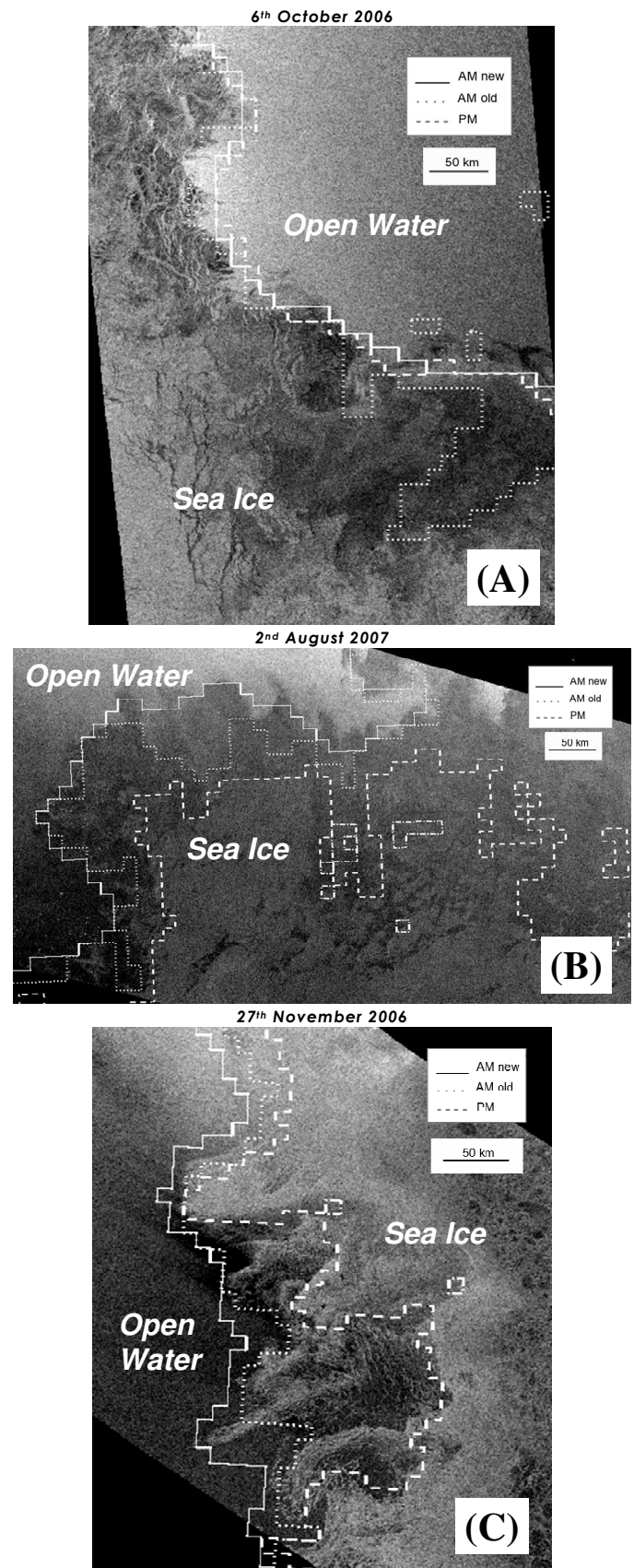


Fig. 9. Sea ice edge from QSCAT-KNMI (AM new, continuous line), QSCAT-SCP (AM old, dotted line) and AMSR-NT2 15% concentration isoline (PM, dashed line) on ASAR Global Monitoring backscatter data. ASAR swath is 500 km wide.

In general, the combined MODIS and ASAR records confirm that all the sea ice detection algorithms under study come to agree within 25 km over areas that do not include mixed ice/water pixels (i.e. thin, low concentration or rotten sea ice). Fig. 9A shows a typical detection discrepancy involving newly formed thin ice off the New Siberian Islands in the Arctic. The QSCAT-SCP algorithm is missing a large tongue of new ice with dark smooth appearance in the image, which is detected by both the QSCAT-KNMI and AMSR-NT2 algorithms. Note that the presence of frequencies of up to 89GHz in passive microwave methods plays favorable to thin ice detection during the growth season due to their lower penetration depth. Fig. 9B shows a typical example of summer biases in the Beaufort Sea, featuring a large expanse of decaying and water saturated ice missed by the AMSR-NT2 algorithm, which the QSCAT-SCP method can only detect partially. Fig. 9C provides another instance of summer biases along the ice edge in the Southern Ocean, this time featuring a number of ice bands of varying concentration. Low concentration, wave battered, decaying and water saturated ice are all examples of diffuse ice edge conditions most likely to be underestimated by passive microwave sea ice concentration algorithms [23].

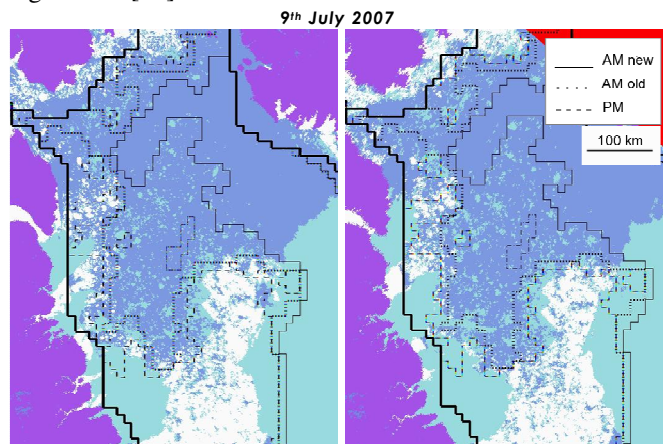


Fig. 10. Sea ice edge from QSCAT-KNMI (AM new, continuous line), QSCAT-SCP (AM old, dotted line) and AMSR-NT2 15% concentration isoline (PM, dashed line) on two sequential MODIS overpasses. MODIS products are cloud masked (cyan) and identify sea ice by its reflectance characteristics.

One last example is shown in Fig. 10, taken from the MODIS sensor over the Baffin Bay and featuring a large but sparse floe field that passes undetected by both the AMSR-NT2 and QSCAT-SCP algorithms. The same scene is observed by MODIS in two sequential overpasses 1/2 hour apart, but the floe field is mistaken for clouds in both cases. Up to this point, we claim to have collected enough evidence to assert that the wintertime performance of the GMF-based Bayesian sea ice detection algorithm with QuikSCAT is comparable to that afforded by passive microwaves, while its summertime performance remains yet unparalleled.

IV. CONCLUSION

This paper details the construction of an improved sea ice detection algorithm for the Seawinds scatterometer on QuikSCAT that exploits detailed knowledge about the ocean wind and sea ice backscatter signatures at Ku-band. The improvement of the new algorithm over earlier scatterometer methods lies in its optimal utilization of the statistical distribution of backscatter in the multidimensional space of measurements; in particular, the introduction of extended ocean wind and sea ice Geophysical Model Functions, leading to enhanced discrimination power using a Bayesian approach. The performance of the new algorithm is validated against existing active and passive microwave sea ice detection algorithms on a global scale, and against high resolution optical and radar imagery at local scales. We observe that seasonal biases between active and passive microwave algorithms arise from their different sensitivities to pixels with mixed volume (sea ice) and surface (open water) scattering signatures. Sea ice species with mixed signatures include new ice formed during the growth season, and low concentration and water saturated sea ice formed during the melt season. In the wintertime, the new QuikSCAT algorithm features an average sea ice edge concentration of 10-15% relative to AMSR-E NT2, improving over previous scatterometer methods in terms of both thin ice detection and random misclassification noise. In the summertime, the performance of the new QuikSCAT algorithm proves robust and reveals the extent of seasonal errors present in other methods. In particular, passive microwave algorithms such as AMSR-E (or SSM/I) NT2 underestimate the extent of summer sea ice by up to 15-20% relative to QuikSCAT, mainly by exclusion of low concentration and water-soaked sea ice conditions. The new QuikSCAT algorithm provides valuable information for the characterization of sea ice during the difficult melting season. It features a rather conservative definition of sea ice edge, one that is more in line with ship observations and well-suited for applications (such as satellite ocean wind or sea surface temperature retrievals) that require a dependable sea ice mask on a daily basis and all year round.

For future work, the GMF-based sea ice detection algorithm could be easily adapted to the Indian Ku-band dual-polarization Oceansat-2 scatterometer. A sea ice detection algorithm for the C-band ASCAT scatterometer on MetOp is already under development, following a similar approach tested on ERS satellites [24]. Misclassification due to rain is less of a problem at C-band, but the effective discrimination between sea ice and ocean wind is more dependent on across-track location for fan beam scatterometers. We also envision the reprocessing of the entire QuikSCAT data record back to 1999 and a critical comparison against the current passive microwave and future ASCAT sea ice extent records.

ACKNOWLEDGMENT

The authors are thankful to Jeroen Verspeek, Jur Vogelzang and Anton Verhoef for their expertise and helpful assistance during the course of this work.

REFERENCES

- [1] Fetterer, F., Knowles, K., Meier, M., Savoie, M., "Sea Ice Index. Boulder, CO: National Snow and Ice Data Center". Digital media. 2002. Updated 2009.
- [2] Cavalieri, D.J., Parkinson, C.L., Gloersen, P., Comiso, J.C., Zwally, H.J., "Deriving long term time series of sea ice cover from satellite passive microwave multisensor datasets", *J. Geophys. Res.*, Vol. 104, No. C7, pp. 15803-15814, 1999.
- [3] Remund, Q.P., Long, D.G., "Sea ice extent mapping using Ku-band scatterometer data", *J. Geophys. Res.*, Vol. 104, No. C5, pp. 11515-11527, 1999.
- [4] Anderson, H.S., Long, D.G., "Sea ice mapping method for SeaWinds", *IEEE Trans. Geosci. Remote Sens.*, Vol. 43(3), 2005.
- [5] Breivik, L.A., Eastwood, S., "Development of a sea ice type product based on the use of QuikSCAT data", Norwegian Meteorology Institute, MERSEA Report, <http://saf.met.no/docs>, 2006.
- [6] Meier, W., Stroeve, J., "Comparison of sea ice extent and ice-edge location estimates from passive microwave and enhanced resolution scatterometer data", *Ann. Glaciology*, No. 48, pp. 65-70, 2008.
- [7] Abreu, R.D., Wilson, K., Arkett, M., Langlois, D., "Evaluating the use of QuikSCAT data for operational sea ice monitoring", *IEEE IGARSS*, Vol.5, pp. 3032 – 3033, 2002.
- [8] Markus, T., Dokken, S., "Evaluation of late summer passive microwave sea ice retrievals", *IEEE Trans. Geosci. Remote Sens.*, Vol.40(2), 2002.
- [9] Stoffelen, A., "Scatterometry", PhD Thesis, U. Utrecht, pp. II-17, 1998.
- [10] Wentz, F.J., Smith, D.K., "A model function for the normalized cross-section at 14 GHz derived from NSCAT observations", *J. Geophys. Res.*, Vol. 104, C5, pp. 11499-11514, 1999.
- [11] Belmonte Rivas, M., Stoffelen, A., "Near Real-Time sea ice discrimination using SeaWinds on QuikSCAT", OSI SAF Visiting Scientist Report, SAF/OSI/CDOP/KNMI/TEC/TN/168, 2009.
- [12] Spencer, M.W., Wu, C., Long, D.G., "Improved resolution backscatter measurements with the SeaWinds Pencil-Beam Scatterometer", *IEEE Trans. Geosci. Remote Sens.*, 38(1), 2000.
- [13] Stoffelen, A., Portabella, M., "On Bayesian scatterometer wind inversion", *IEEE Trans. Geosci. Remote Sens.*, Vol. 44(6):1523-1533, 2006.
- [14] Portabella, M., Stoffelen, A., "Scatterometer backscatter uncertainty due to wind variability", *IEEE Trans. Geosci. Remote Sens.*, Vol. 44(11): 3356-3362, 2006.
- [15] Leidner, S.M., Hoffman, R.N., Augenbaum, J., "SeaWinds Scatterometer Real-Time BUFR Geophysical Data Product, User's Guide", Version 2.3.0, NOAA/NESDIS, 2000.
- [16] Markus, T., Cavalieri, D.J., "An enhancement of the NASA Team sea ice algorithm", *IEEE Trans. Geosci. Remote Sens.*, Vol. 38(3): 1387-1398, 2000.
- [17] Comiso, J.C., Cavalieri, D.J., Markus, T., "Sea ice concentration, ice temperature and snow depth using AMSR-E data", *IEEE Trans. Geosci. Remote Sens.*, Vol. 41(2): 243-252, 2003.
- [18] Cavalieri, D., and J. Comiso, "AMSR-E/Aqua Daily L3 12.5 km Tb, Sea Ice Conc., & Snow Depth Polar Grids V001", March to June 2004. Boulder, CO, USA: National Snow and Ice Data Center. Digital media, 2004.
- [19] Draper, D.W., Long, D.G., "Evaluating the effect of rain on SeaWinds scatterometer measurements", *J. Geophys. Res.*, Vol. 109, doi:10.1029/2002JC001741, 2004.
- [20] Haarpaintner, J., Tonboe, R.T., Long, D.G., VanWoert, M.L., "Automatic detection and validity of the sea ice edge: an application of enhanced resolution QuikSCAT/SeaWinds data", *IEEE Trans. Geosci. Remote Sens.*, Vol. 42(7): 1433-1443, 2004.
- [21] Heinrichs, J.F., Cavalieri, D.J., Markus, T., "Assessment of the AMSR sea ice concentration product at the ice edge using RADARSAT-1 and MODIS images", *IEEE Trans. Geosci. Remote Sens.*, Vol.44(11), 2006.
- [22] Riggs, G.A., Hall, D.K., Ackerman, S.A., "Sea ice extent and classification mapping with the Moderate Resolution Imaging Spectroradiometer airborne simulator", *Remote Sens. Environ.*, 68:152-163, 1999.
- [23] Worby, A.P., Comiso, J.C., "Studies of the Antarctic sea ice edge and ice extent from satellite and ship observations", *Remote Sens. Environ.*, No. 92: 98-111, 2004.
- [24] Stoffelen, A., "Scatterometer applications in the European Seas" in *Remote Sensing of the European Seas*, V. Barale and M. Gade (Eds.), Springer Netherlands, pp. 269-282, 2008.

Maria Belmonte Rivas received the B.S. degree in physics (meteorology) from the Universidad Complutense de Madrid, Spain, in 1999 and the M.S. and Ph.D. degrees in aerospace engineering from the University of Colorado at Boulder in 2007. From 2000 to 2007, she was involved in the analysis of Global Positioning System (GPS) reflections for ocean altimetry, ocean wind and the characterization of polar sea ice. From 2007 to 2010, she worked at the Royal Netherlands Meteorological Institute (KNMI) in the satellite wind remote sensing group. She is currently stationed at the National Center for Atmospheric Research (NCAR) in Boulder, working on improved atmospheric retrievals from the EOS Aura infrared limb sounder (HIRDLS).

Ad Stoffelen leads a group on satellite wind remote sensing at the Royal Netherlands Meteorological Institute (KNMI). His main interests lie in scatterometry and Doppler Wind Lidar (DWL), where he is responsible for the winds of the ASCAT scatterometer on EUMETSAT's MetOp and involved in the development of the ground processing of the forthcoming ESA Aeolus DWL mission. Other interests are in data assimilation in meteorological models.